*J. Fluid Mech.* (2008), *vol.* 594, *pp.* 183–208. © 2008 Cambridge University Press
doi:10.1017/S0022112007008968 Printed in the United Kingdom


# Experiments on gas transfer at the air–water interface induced by oscillating grid turbulence

HERLINA AND G. H. JIRKA
Institute for Hydromechanics, University of Karlsruhe, Germany

(Received 10 October 2006 and in revised form 29 August 2007)

The gas transfer process across the air–water interface in a turbulent flow environment, with the turbulence generated in the water phase far away from the surface, was experimentally investigated for varying turbulent Reynolds numbers $Re_T$ ranging between 260 and 780. The experiments were performed in a grid-stirred tank using a combined particle image velocimetry – laser induced fluorescence (PIV-LIF) technique, which enables synoptic measurements of two-dimensional velocity and dissolved gas concentration fields. The visualization of the velocity and concentration fields provided direct insight into the gas transfer mechanisms. The high data resolution allowed detailed quantification of the gas concentration distribution (i.e. mean and turbulent fluctuation characteristics) within the thin aqueous boundary layer as well as revealing the near-surface hydrodynamics. The normalized concentration profiles show that as $Re_T$ increases, the rate of concentration decay into the bulk becomes slower. Independent benchmark data for the transfer velocity $K_L$ were obtained and their normalized values ($K_L Sc^{0.5}/u_{HT}$) depend on $Re_T$ with exponent $-0.25$. The spectra of the covariance term $c'w'$ indicate that the contribution of $c'w'$ is larger in the lower-frequency region for cases with small $Re_T$, whereas for the other cases with higher $Re_T$, the contribution of $c'w'$ appears to be larger in the higher-frequency region (small eddies). These interrelated facts suggest that the gas transfer process is controlled by a spectrum of different eddy sizes and the gas transfer at different turbulence levels can be associated with certain dominant eddy sizes. The normalized mean turbulent flux $\overline{c'w'}$ profiles increase from around 0 at the interface to about 1 within a depth of approximately $2\delta_e$, where $\delta_e$ is the thickness of the gas boundary layer. The measured turbulent flux ($c'w'$) is of the same order as the total flux ($\bar{j}$), which shows that the contribution of $c'w'$ to the total flux is significant.

## 1. Introduction

Gas transfer across the air–water interface plays an important role in many environmental and industrial systems. The problem areas range from natural geochemical cycling of materials to anthropogenic water quality (e.g. reaeration) problems in aquatic systems to applications in industrial facilities. Recently, there has been intense interest in problems associated with the transport of greenhouse gases (in particular carbon dioxide, $CO_2$), which has a major effect on the global climate change. The major sink (up to 40 %) for $CO_2$ is transfer into the oceans (Donelan & Wanninkhof 2002). Improved understanding of the gas exchange across the air–sea interface is thus important since the process governs the balance of $CO_2$ cycling. The classical interest in the subject of gas transfer across free surfaces arose from the need to predict the oxygen dynamics in rivers downstream of a pollutant

source (mostly organic waste). The bio-degradation processes of the organic wastes, which consume oxygen at a very high rate, lead to a DO (dissolved oxygen) deficit in the river. Particularly in streams, the primary source for replenishing the DO concentration is reaeration. In-depth knowledge of the gas absorption process to allow accurate prediction of the reaeration rate is thus an essential element of water quality modelling. The main source of turbulence in flowing streams comes from the shear stress at the bottom. The other two turbulent driving mechanisms typical for environmental conditions are wind-induced turbulence and buoyant-convection turbulence. The present study focuses on the gas transfer process in a water environment dominated by bottom-shear-induced turbulence. In inland water bodies, the combined effects of wind-shear- and bottom-shear-induced turbulence are important. Of course, wind is most effective in enhancing the gas transfer process near the air–water interface. However, for cases with weak wind speeds, the effect of bottom-shear-induced turbulence becomes increasingly important, if not dominant.

The gas transfer process is controlled by a complex interaction between molecular diffusion and turbulent exchange processes near the interface, modified additionally by organic films or microlayers ('surfactants') that often exist in natural waters. Assuming that the gas transfer process is horizontally homogeneous, the total gas flux $\overline{j}$ can be written as

$$\overline{j} = -D\frac{\partial \overline{c}}{\partial z} + \overline{c'w'}, \tag{1.1}$$

where $D$ is the molecular diffusivity, $\overline{c}$ is the mean concentration, $c'$ and $w'$ are the concentration and velocity fluctuation, respectively, and $z$ denotes the vertical direction (with the convention that positive is in the downward direction). The first term on the right-hand side represents the molecular diffusion and the second correlation term the turbulent mass transport. For gases with low solubility (such as $O_2$, CO, $CO_2$, NO), the transfer process is governed by resistance within a very thin layer on the liquid side. The limited thickness of this aqueous boundary layer (typically tens to hundreds of micrometres) has been until now the most severe obstacle in understanding the actual mechanisms of gas transfer in turbulent environments. Therefore, most previous studies focused on quantifying the gas transfer rate or transfer velocity $K_L$, defined as $K_L = j/(C_s - C_b)$ where $j$ is the gas flux across the interface, $C_b$ is the dissolved gas concentration in the bulk region and $C_s$ is the equilibrium gas concentration given by Henry's law. Many workers attempted to find a practical relation between $K_L$ and some global flow properties, such as the mean velocity, slope or water depth (e.g. O'Connor & Dobbins 1956; Churchill 1961; Thackston & Krenkel 1969; Plate & Friedrich 1984; Gulliver & Halverson 1989) or some more specific flow parameters, such as bed roughness, wave slope or surface divergence (e.g. Moog & Jirka 2002; Turney, Smith & Banerjee 2005). Other workers developed conceptual models to describe the transfer process. The first conceptual model was the 'film-model' (Lewis & Whitman 1924). The model assumed a stagnant film on each side of the interface where molecular diffusion is the controlling factor in the transport process, leading to the relation $K_L = D/\delta$, where $\delta$ is the thickness of the stagnant film. It is clear that the 'film model' oversimplifies the actual mechanisms of the transfer process. However, the linear assumption was sufficient for their actual purpose, which was to estimate the relative importance of gas-phase and liquid-phase resistances between different gases with varying solubility. A number of experiments (see e.g. McCready, Vassiliadou & Hanratty 1986) have shown that the functional dependence between $K_L$ and $D$ was never linear. This led Higbie (1935) to develop a 'penetration model' which is based

on a so-called surface renewal effect. His idea was that the turbulence in the bulk region of the fluid would bring up fresh packages of liquid to the surface, where gas transfer takes place for a certain renewal time $T$. Danckwerts (1951) modified Higbie's penetration model by allowing the constant renewal time $T$ to follow an exponential probability distribution of surface renewal rate $r$, so that $K_L \approx \sqrt{Dr}$. Other conceptual models have been proposed by, for example, O'Connor & Dobbins (1956) and Harriott (1962). All renewal models have shown that the transfer velocity $K_L$ is related to the square root of the molecular diffusivity $D$ and a renewal rate $r$. However, the hydrodynamics affecting the gas transfer process are still hidden in the $r$ term which must be determined experimentally for individual turbulence conditions. Some workers tried to relate the unknown term $r$ to measurable hydrodynamic parameters of the flow. With this approach, Fortescue & Pearson (1967) proposed the 'large-eddy model'. They assumed that the largest turbulent eddies dominate the gas transfer process and thus $r$ can be estimated by $u_L/L$, where $u_L$ is the root mean square turbulent fluctuation and $L$ the turbulent integral length scale. The relation $K_L \approx \sqrt{Du_L/L}$ then applies. On the other hand, Banerjee, Rhodes & Scott (1968) and Lamont & Scott (1970) suggested that small eddies are the dominant mechanism controlling the transfer process and the term $r$ could be approximated by $(\epsilon/\nu)^{1/2}$ in which $\epsilon$ is the turbulent energy dissipation rate near the interface and $\nu$ the kinematic viscosity. This yields the relation $K_L \approx \sqrt{D}[\epsilon/\nu]^{1/4}$, the so-called 'small-eddy model'. The prediction of $K_L$ using the large-eddy model and the small-eddy model can also be written in the form $K_L Sc^{0.5}/u_L \propto Re_T^{-0.5}$ and $K_L Sc^{0.5}/u_L \propto Re_T^{-0.25}$, respectively. Theofanus, Houze & Brumfield (1976) tried to interpret the differences on the power dependence of the turbulent Reynolds number as being dependent on the range of the intensity level of the turbulence involved (see also Theofanus 1984). They proposed a two-regime model in which the large-eddy model is relevant at low turbulent Reynolds numbers $Re_T$ and the small-eddy model at high $Re_T$. Another conceptual model originated from the numerical investigations performed by McCready *et al.* (1986). They showed that the surface divergence played an important role in the interfacial gas transfer process.

Until the late 1980s, the conceptual models were not supported by detailed near-surface hydrodynamic measurements. Brumley & Jirka (1987) were the first to perform such measurements in a water environment dominated by bottom-shear-induced turbulence, by employing a grid-stirred tank system. On the basis of the Hunt & Graham (1978) theory, they were able to define different hydrodynamic layers near the free surface that could be inferred based on their measurements as well as from scaling arguments (Brumley & Jirka 1988). Tamburrino & Gulliver (2002), McKenna & McGills (2002, 2004b), Sugihara & Tsumori (2005) resolved the near-surface velocity fields using a particle image velocimetry (PIV) technique. Their results showed that the surface divergence provided a relationship for $K_L$ that accounted for the interfacial contamination and was independent of the flow regime.

Equation (1.1) shows that in order to understand fully the physical mechanisms that control the gas transfer process, it is essential to resolve the concentration characteristics near the surface as well. Detailed mapping of the concentration distribution directly below the water surface in a far-field homogeneous turbulent water environment was first reported by Jirka & Ho (1990); Chu & Jirka (1992). They employed an oxygen microprobe that was capable of following fluctuations in the concentration $O_2$. They were able to show that the mean concentration follows an exponential distribution. With the development of imaging techniques, especially laser induced fluorescence (LIF), further detailed concentration measurements within the

boundary layer could be performed (Wolff & Hanratty 1994; Münsterer, Mayer & Jähne 1995; Woodrow & Duke 2002). Parallel to the laboratory experiments, numerical simulations have also been conducted in order to understand mass transfer processes using DNS (e.g. Pan & Banerjee 1995; Kunugi & Satake 2002; Lakehal, Fulgosi & Yadigaroglu 2003) and LES (e.g. Magnaudet & Calmet 2006).

Despite these intensive research efforts, the turbulent mass transport term $c'w'$ is typically not known and has to be modelled. Direct quantification of $c'w'$ is difficult, but still possible through simultaneous measurements of the gas concentration fluctuations and velocity fluctuations near the surface region (known as the eddy correlation method). Attempts to measure the turbulent mass fluxes across the interface under homogeneous isotropic turbulence generated far away from the interface have been made by Chu & Jirka (1992) and Atmane & George (2002). However, their results were inconclusive, most probably owing to the intrusive and spatially non-coincident measurement techniques. In the first step of this study, LIF gas concentration measurements were performed (Herlina & Jirka 2004). In the present paper, as a second step, the same LIF set-up is combined with the PIV technique. This enables simultaneous and spatially synoptic measurements with high resolution of two-dimensional velocity and concentration fields, allowing detailed mapping of the concentration and velocity fields and also, for the first time, reliable direct quantification of the turbulent mass flux $c'w'$.

## 2. Experimental set-up and conditions

### 2.1. *Turbulence generation and measurement technique*

A grid-stirred tank system was employed to generate turbulence with known reproducible scales (i.e. well-controlled conditions). In such a system, the turbulence is generated away from the surface and decays as it diffuses towards the interface. Despite the differences of turbulence generation, the interaction between the interface and the turbulence has similar characteristics to that occurring at the water surface in flowing streams. The turbulence characteristics generated by grid-stirred systems have been studied in depth by Thompson & Turner (1975) and Hopfinger & Toly (1976), and also by Matsunaga *et al.* (1999) and McKenna & McGillis (2004*a*). Brumley & Jirka (1987), Thompson & Turner (1975) and Chu & Jirka (1992) have shown that the grid-stirred tank is suitable for investigations in the area of gas transfer.

Figure 1 shows a schematic illustration of the experimental set-up. The tank was made of Perspex with inner dimensions of $50 \times 50 \times 65\,\mathrm{cm}^3$. Glass windows were installed in the sidewalls to enhance optical access for laser techniques (PIV and LIF). The oscillating grid consisted of an aluminium plate perforated to form a $7\,\mathrm{bar} \times 7\,\mathrm{bar}$ grid. The centre to centre mesh size $M$ was 62.5 mm and the hole size was $50 \times 50\,\mathrm{mm}^2$, resulting in a mesh solidity of 36 %, which is optimal to avoid secondary motions and inhomogeneity (Hopfinger & Toly 1976).

Two non-invasive measurement techniques, PIV and LIF, were employed to measure planar velocity and gas concentration fields near the interface, respectively. The LIF technique developed by Vaughan & Weber (1970) is based on the oxygen quenching phenomenon and uses pyrene butyric acid (PBA) as dye tracer. This method does not involve any chemical reactions and the absorbance of the PBA solution is independent of external parameters such as pH value. The major advantage of the PIV and LIF techniques is that they can be coupled providing a simultaneous measurements of

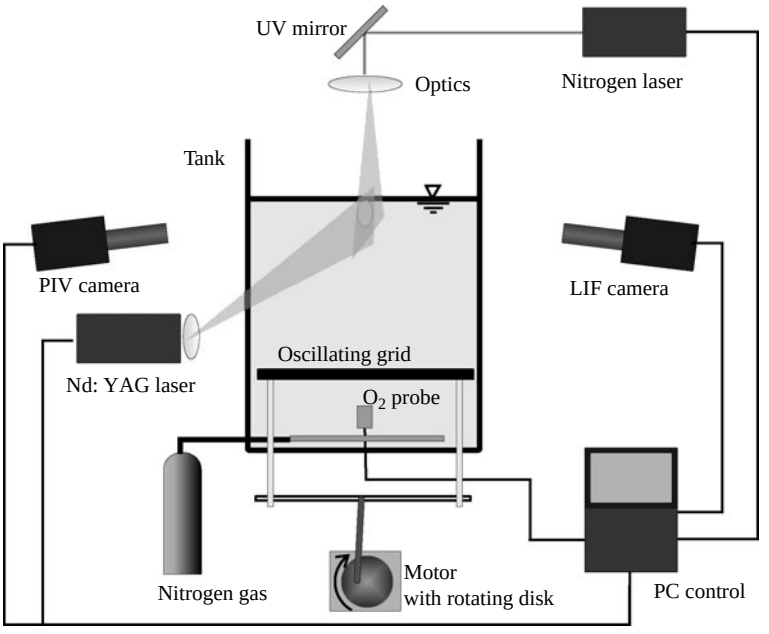


FIGURE 1. Schematic illustration of the experimental set-up. The tank has inner dimensions of $50 \times 50 \times 65\,\mathrm{cm}^3$. The main components of the optical set-up consisted of an Nd: YAG laser for PIV, a nitrogen laser for LIF and two CCD cameras. The vertical oscillation of the grid was varied in the range 2 to 6 Hz corresponding to $Re_T = 260$ to 780.

velocity and concentration that enables direct quantification of the turbulent mass flux ($c'w'$ in (1.1)).

The main components of the coupled PIV-LIF set-up (figure 1) consisted of tracers, an illumination system (lasers) and a recording system (cameras). Polyamid particles with nominal diameter of 10 μm and an optimum PBA concentration of $2 \times 10^{-5}$ molar were used as PIV and LIF tracers, respectively. A lower PBA concentration resulted in a fluorescence intensity that was too weak, whereas higher concentration made the solution too opaque. To evaluate the effect of PIV particles on the LIF images, additional experiments in which only the gas concentration was measured (with no PIV particles) were performed. Comparing the results with those obtained from the simultaneous PIV-LIF measurements, it could be shown that the effect of the particle interference in the LIF images was negligible (Herlina 2005).

The PIV laser was a dual-cavity Q-switched Nd:YAG laser which emitted pulse-pairs with an energy level of 25 mJ per pulse at a wavelength of 532 nm (green). The pulse-pair interval was set between 3 and 18 ms. For LIF, a pulsed nitrogen laser (MNL 801) with a mean energy power of 0.4 mJ at 337.1 nm was used. Both laser beams were directed into the centre of the test tank using UV-mirrors and expanded into light sheets. The PIV laser entered the test tank from the sidewall and the LIF laser from above the water surface. A disadvantage of directing the laser sheet from above the water surface arose when dust particles happened to float to the water surface and partially block the laser light as it crossed the water surface. This led to additional noise in the recorded intensity images. An ideal configuration would be guiding the LIF laser light also through the sidewalls. However, a nitrogen laser with a very high power would be required so that sufficient intensity still reaches

the measurement area. For the LIF laser power available, the present illumination configuration was an optimal trade-off.

The illuminated flow fields were captured using two SensiCam charge coupled device (CCD) cameras, each with a resolution of $1280 \times 1240$ pixels and a grey-scale depth of 12 bits. The recording rate was limited by the CCD camera transfer rate which is 4 Hz (double frames). The PBA fluorescence lies between 370 and 410 nm and the scattered light from the PIV laser was at 532 nm. An optical bandpass filter was mounted in front of each camera to ensure that only the fluorescent light and scattered Nd:YAG laser light could reach the camera chips from the LIF and PIV camera, respectively. The PIV camera was positioned at the opposite side of the LIF camera. The measurement window of the PIV camera was approximately $20 \times 20\,\mathrm{mm}^2$ so that it covered the $10 \times 10\,\mathrm{mm}^2$ area of the LIF camera. A measurement window smaller than $20 \times 20\,\mathrm{mm}^2$ for the PIV camera was not possible because more seeding particles would be required which would make the water too opaque. In addition, the noise in the fluorescence signals would no longer be negligible when too many seeding particles were present in the LIF images. In order to zoom into the small investigation areas near the surface from a distance of about 50 cm, two macro objectives Componon-S 5.6/135 from Schneider Optics were used. Both cameras were tilted about 10° so that the viewing point was from slightly below the water surface. This was necessary to eliminate interference from the water-surface meniscus at the sidewall facing the camera.

The synchronization of the cameras and lasers through a programmable timing unit (PTU) board was managed using the DaVis software developed by LaVision. DaVis also provides the cross-correlation algorithm for computing the vector fields. From each PIV image pair, a vector map of $80 \times 64$ points was obtained using a $32 \times 32$ pixel interrogation area with 50 % overlap. The algorithm for the LIF image processing has been detailed in Herlina & Jirka (2004).

### 2.2. *Experimental conditions*

The experiments were performed for five different levels of turbulence intensities characterized using the turbulent Reynolds number $Re_T$

$$Re_T = \frac{u'_\infty 2L_\infty}{\nu}, \tag{2.1}$$

where $u'_\infty$ is the far-field turbulence intensity, $L_\infty$ the longitudinal integral length scale and $\nu$ is the kinematic viscosity (Brumley & Jirka 1987). The term $u'_\infty$ is estimated using the relation given by Hopfinger & Toly (1976) ($u_{HT} = cfS^{1.5}M^{0.5}z_s^{-1}$, with $f$ being the frequency of the oscillation, $S$ the stroke, $z_s$ the distance from the centre of the stroke towards the water surface and $c = 0.25$). The length scale can be approximated by $L_\infty = 0.1z_s$ (Thompson & Turner 1975). The different levels of turbulence intensities were controlled by varying the frequency of the oscillating grid from 2 to 6 Hz which corresponded to $Re_T$ (equation (2.1)) from 260 to 780. The turbulence characteristics of the present grid-stirred tank system have been evaluated through independent PIV measurements in the bulk region extending from near the grid up to 3 cm below the water surface. The evaluation showed that the decay of the turbulence fluctuations ($u'$ and $w'$) were in close agreement with Hopfinger & Toly (1976), the growth of $L_\infty$ was comparable with the estimation of Thompson & Turner (1975) and the turbulence generated was horizontally homogeneous and fully three-dimensional (Herlina 2005, pp. 52–66). As has been shown by McKenna & McGillis (2004*a*), it is extremely difficult to avoid secondary circulation flows in grid-stirred

| Experiment series | Frequency $f$(Hz) | Water depth (mm) | $T$ (°C) | $L_\infty$ (mm) | $u'_\infty$ (mm s$^{-1}$) | $Re_T$ | $C_b$ (mg l$^{-1}$) |
|---|---|---|---|---|---|---|---|
| CV1 | 2 | 486 | 14.3 | 28.6 | 4.6 | 260 | 1.02 |
| CV2 | 3 | 485 | 14.4 | 28.5 | 6.9 | 390 | 0.97 |
| CV3 | 4 | 485 | 14.8 | 28.5 | 9.1 | 520 | 0.98 |
| CV4 | 5 | 490 | 15.0 | 29.0 | 11.2 | 650 | 0.77 |
| CV5 | 6 | 480 | 15.3 | 28.0 | 14.0 | 780 | 0.89 |

TABLE 1. Experimental parameters for the simultaneous PIV-LIF and gas transfer measurements (CV-series). In all experiments, the stroke of the oscillating grid was 5 cm. For the calculation of $u'_\infty = u_{HT}$, $c = 0.233$ determined from the independent PIV bulk measurements was used.

tank systems. The estimated mean flow in the tank was about 1 – 4 mm s$^{-1}$, which was sufficiently lower than the turbulence fluctuations generated by the system.

The chosen $Re_T$ investigated in this study spanned both low- and high-turbulence flow regimes suggested by Theofanus (1984) and thus it was expected to cover a sufficiently wide spectrum of turbulent eddies. In addition, the turbulence levels produced corresponded roughly to stream flows with $u_*$ ranging between 0.65 and 2 cm s$^{-1}$. Typical values in nature are mostly higher than 2 cm s$^{-1}$. However, natural streams with this lower range of $u_*$ do exist, such as the Eaton Nord River in Canada with $u_* = 0.5$ to 1.3 cm s$^{-1}$ (Roy *et al.* 2004). The specific experimental conditions such as temperature $T$, water depth and bulk concentration $C_b$, are given in table 1.

The interfacial gas transfer process was induced by forcing a concentration gradient between the interface and the water in the bulk region. This was achieved through nitrogen bubbling which purged the dissolved oxygen. To ensure stable turbulence conditions, the measurements commenced at least 20–30 min after the grid started to oscillate. The undulations at the water surface were typically smaller than 30 μm so that it could be considered as flat.

## 3. Results

### 3.1. *Qualitative observations of instantaneous concentration and velocity fields*

Figures 2 and 3 show examples of 8 successive images of the simultaneous concentration and velocity maps taken from series CV2 and CV3, respectively. The horizontal axis $x$ indicates the distance from the sidewall and the vertical axis $z$ indicates the depth from the water surface. The dark and light colour scaling in the concentration images correspond to regions with high and low oxygen concentration, respectively. The darkest layer occurs at the water surface where the oxygen concentration reaches saturation. In the vicinity of the interface, a very thin dark layer indicates the boundary layer in which the oxygen concentration decreases rapidly from saturated to the bulk concentration. Below this boundary layer, the images are dominated by light colour corresponding to the low oxygen concentration in the bulk region that is constantly being mixed by the turbulence generated by the oscillating grid.

The superimposition of the velocity maps onto the concentration maps gives a better insight into the interaction between the turbulent flow field and gas transfer process. For example, in figures 2 and 3 (images 108–114), a transport process initiated by an eddy structure can be visualized. The turbulent structure is peeling off portions of the surface layer, transporting fluid with higher oxygen concentration into the bulk region.

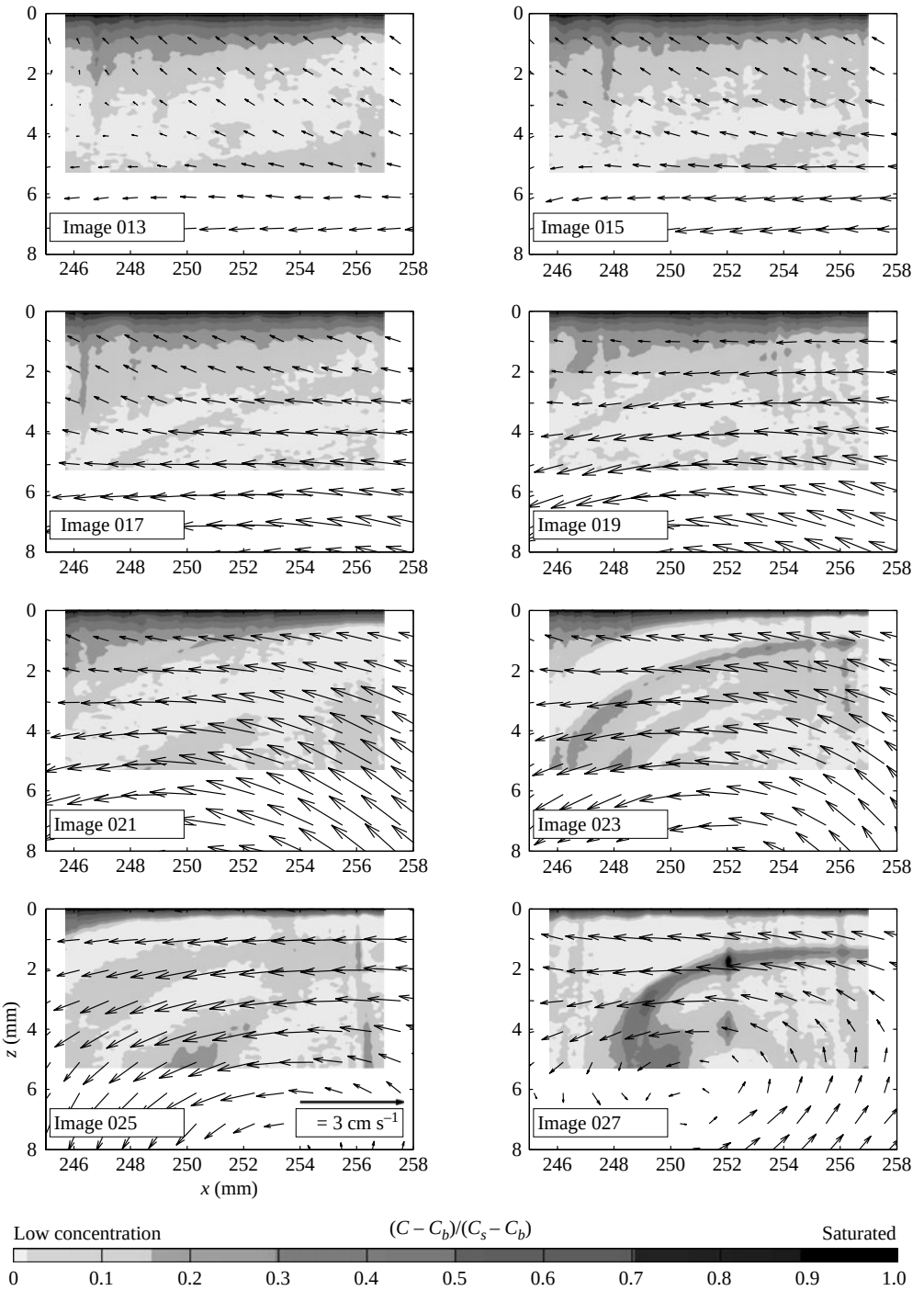


FIGURE 2. Synoptic sequence of oxygen contour map and vector map from the simultaneous PIV-LIF measurements, taken from CV2 ($Re_T = 390$). For clarity, only every third vector is shown. The time interval between the images shown is 0.5 s. In this sequence, a large-scale turbulent structure is peeling off portions of the surface layer, transporting fluid with higher oxygen concentration into the bulk region (surface renewal events).

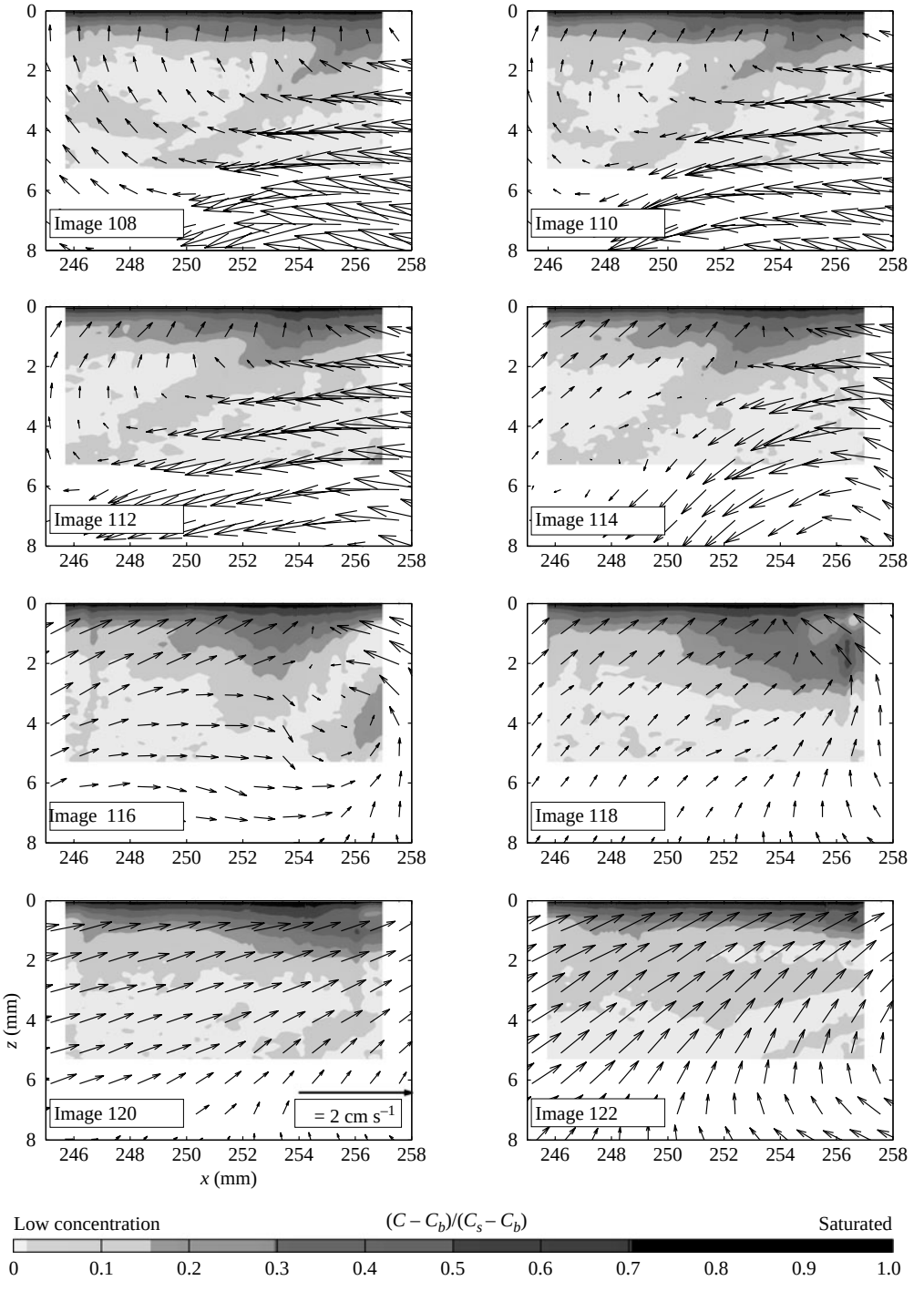


FIGURE 3. Synoptic sequence of oxygen contour map and vector map from the simultaneous PIV-LIF measurements, taken from CV3 ($Re_T = 520$). For clarity, only every third vector is shown. The time interval between the shown images is 0.5 s. In images 108–114, a surface renewal event is observed. In image 116, an eddy of smaller size is visible.

These surface renewal events are associated with upwelling turbulent structures (also referred to as splats or updraughts, Banerjee *et al.* 2004) and downwelling structures (antisplats or downdraughts). Further discussion on the upwelling and downwelling motions is given in § 3.6.1. It is observed that the surface renewal events occur several times in all sequences measured with different turbulence levels.

The turbulent eddies initiating the peeling process are obviously larger than the observation windows. As mentioned, our focus is on elucidating the concentration and hydrodynamics properties within the limited boundary layer, therefore we zoomed into an area as small as $5 \times 10\,\mathrm{mm}^2$. The trade off between the high resolution we achieved and the size of the observation window is that we were able to visualize small- to intermediate-scale structures, but we could not fully capture the large-scale turbulent structures. A good complement to the present study is the investigation by Magnaudet & Calmet (2006) using LES numerical simulations. Their investigation window was $15L_\infty$ in the horizontal direction and $6L_\infty$ in the vertical direction (about 40 times larger than ours). Within their larger window, they could resolve the large-scale turbulent upwelling and downwelling motions. They found that the typical horizontal size of the structures is about the turbulence macroscale $2L_\infty$. From their iso-contours of $c'$, they observed that high-concentration structures driven by downwelling motions were typically in the form of needles that penetrate into the bulk region.

In figure 3 (image 116), an eddy of smaller size could be observed. For comparison, the characteristic length scale of the smallest turbulent eddies, the Kolmogorov scale $\eta$, is estimated as $\eta = 2L_\infty Re_T^{-3/4}$ (Brumley & Jirka 1987). Based on this estimation, the Kolmogorov scales for the cases shown in figures 2 (CV2) and 3 (CV3) are about 0.65 mm and 0.52 mm, respectively. The large structures, on the other hand, would be theoretically of the order of the integral scale $L_\infty = 28.5\,\mathrm{mm}$. The eddy captured in figure 3 (image 116) is therefore of intermediate scale. Herlina & Jirka (2004) discussed the qualitative observations obtained from the first LIF measurements conducted within this study. In that paper, sequences with eddies of relatively small sizes were reported. These sequences provided good visualizations of the modification of the turbulent structure approaching the boundary. It could be shown that as soon as the structure impinges on the water surface, the vertical growth of the structure is inhibited and consequently it undergoes horizontal stretching and finally diffuses. From the visual observations, it seems that a wide spectrum of eddy scales contribute to the transfer process.

### 3.2. *Boundary-layer thickness*

The instantaneous concentration images (figures 2 and 3) show that the turbulent structures have a direct influence on the boundary-layer thickness. Figures 4(*a*) and 4(*b*) represent this temporal variation of the boundary-layer thickness $\delta_g$ at one selected point ($x = 253.7\,\mathrm{mm}$) for measurements with the lowest $Re_T$ and highest $Re_T$, respectively. The thickness $\delta_g$ is defined as the intercept of the instantaneous tangent of the concentration profile at the interface with the ordinate, $\delta_g = (C_s - C_b)/(-\partial c/\partial z|_{z=0})$. The plots show a lower baseline of $\delta_g$, indicating the persistence of a concentration boundary layer (no breaking of the interface) throughout the present experiments. The large deviations from the baseline are related to the hydrodynamic actions as indicated by the associated $w'$ plotted on the right-hand axes in figure 4. Upwelling eddy motions ($w' < 0$) cause a thinning of the boundary layer, whereas downwelling eddy motions ($w' > 0$), which are peeling or sweeping part of the concentration boundary layer, thicken the boundary layer. This can also be observed more clearly,

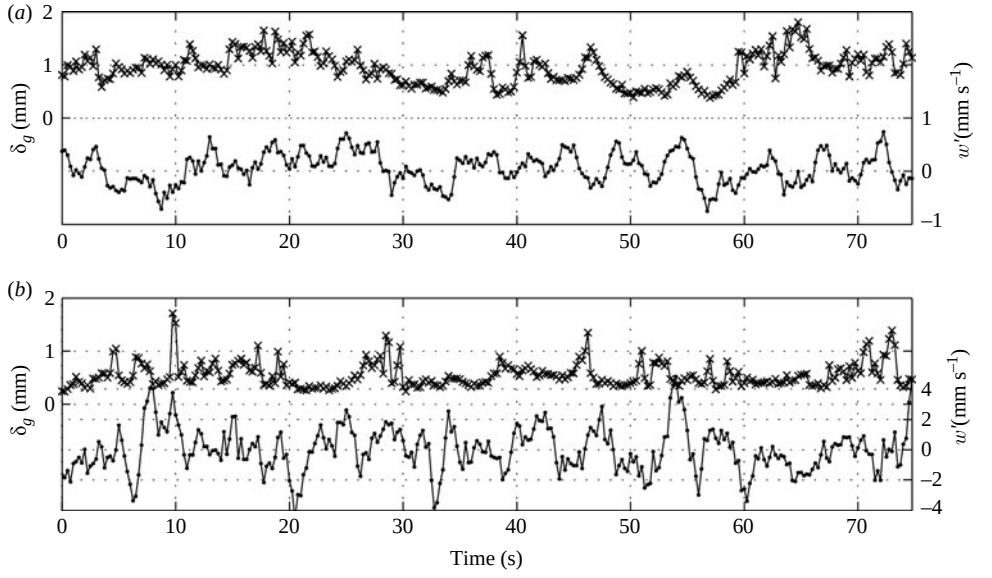


FIGURE 4. Time series of local boundary-layer thickness. (*a*) $Re_T = 260$ and (*b*) with $Re_T = 780$. Also shown are the smoothed vertical fluctuations $w'$; $w' > 0$ and $w' < 0$ indicate downwelling and upwelling eddy motions, respectively.

for example, in figure 2, as soon as an upwelling eddy approaches the interface (images 21 to 25), the boundary layer consequently becomes thinner as compared to the boundary layer in images 15 to 17. These energetic hydrodynamic actions cause temporal changes in the absorption rate. In the mean, the boundary layer is obviously thinner for the case with higher $Re_T$, leading to a higher transfer rate.

The mean boundary-layer thickness $\delta_e$ can be defined as the depth $z$ where the value of the normalized concentration $(C - C_b)/(C_s - C_b)$ is equal to 1/e. In figure 5(*a*), the mean $\delta_e$ are plotted against the square root of the interfacial kinetic energy $\sqrt{k_s}$ ($k_s = 0.5(u_{HT}^2 + u_{HT}^2)$). Consistent with figure 4, this shows that the boundary layer is limited by higher turbulence intensities. The thickness decreases from about 800 µm for $Re_T = 260$ to 300 µm for $Re_T = 780$. Data from Atmane & George (2002) are comparable with the present data although the turbulence-generation technique was somewhat different (up-flowing micro jets), whereas the data from Chu & Jirka (1992) show smaller values compared with the present study, perhaps owing to the invasive oxygen probes.

The large-scale turbulent motions just outside the concentration boundary layer give rise to an outer diffusive sublayer that can be estimated with $L_D = 2L_\infty Sc^{-1/2} Re_T^{-1/2}$ (Brumley & Jirka 1988). Figure 5(*b*) shows the outer diffusive sublayer for the present grid conditions plotted against the measured boundary layer $\delta_e$. The solid line indicates the relationship

$$\delta_e = cL_\infty Sc^{-1/2} Re_T^{-1/2}, \tag{3.1}$$

with $c$ a constant. Excluding data point $Re_T = 260$, a $c$ value of 3.8 gives the best fit to (3.1). For comparison, Chu & Jirka (1992) obtained a $c$ value of 2 to 3 and they concluded that the gas transfer process should be dominated by the large eddies at least in their measured range of turbulent Reynolds number (80 to 660).

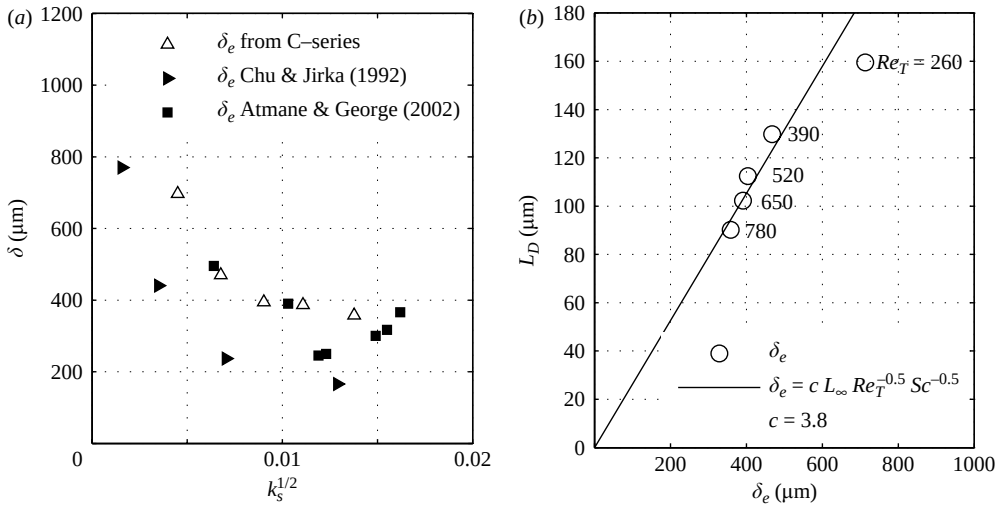


FIGURE 5. (*a*) Measured boundary-layer thickness $\delta_e$ plotted against the square root of the interfacial turbulent kinetic energy $\sqrt{k_s}$. (*b*) Outer diffusive sublayer *vs.* boundary-layer thickness.

### 3.3. *Mean and turbulence characteristics of concentration*

Statistical analyses were performed over the 900 instantaneous images acquired in each experimental series. The information at the edges of the LIF images, were discarded in order to eliminate the area with low grey-scale contrast. Hence, an area of about $500 \times 500$ pixels from the total capacity of $1280 \times 1024$ pixels was used in the analysis. The mean profiles were obtained by temporally averaging and then spatially averaging the 900 instantaneous quantities.

#### 3.3.1. *Mean profiles*

The oxygen concentration in the bulk region $C_b$ and at the interface $C_s$ differ slightly in each experiment. Therefore, for better interpretation, it is convenient to present the profiles in a non-dimensional form of $(C - C_b)/(C_s - C_b)$ against $z/\delta_e$ (figure 6). The data points from Chu & Jirka (1992) with $Re_T = 360$ and Atmane & George (2002) are incorporated in the figure, which highlights the advantage of the non-intrusive LIF quenching method over their point-based oxygen microprobe technique. The solid and dashed lines indicate the theoretical predictions of the concentration distribution for a mobile interface reported in Jähne & Haussecker (1998). The theoretical profiles were obtained by solving the mass flux equation using the surface renewal model (with the assumption that the larger turbulent scales play a dominant role) and a small eddy-turbulent diffusion model. The major difference between these two predictions is that the profile predicted by the surface renewal model decreases much faster towards the concentration in the bulk region. The mean distribution obtained by Chu & Jirka (1992) and Atmane & George (2002) showed relatively good agreement with the surface renewal model. On the other hand, our measured profiles fall between the two theoretical predictions, with the following tendency, as the turbulent Reynolds number increases, the spatial drop-off of the concentration into the bulk is slower. In line with the visual observations, the results suggest that the gas transfer is controlled by a spectrum of different eddy sizes. It seems that the gas transfer at different turbulence levels can be associated with a certain eddy size. At very high turbulence levels, the

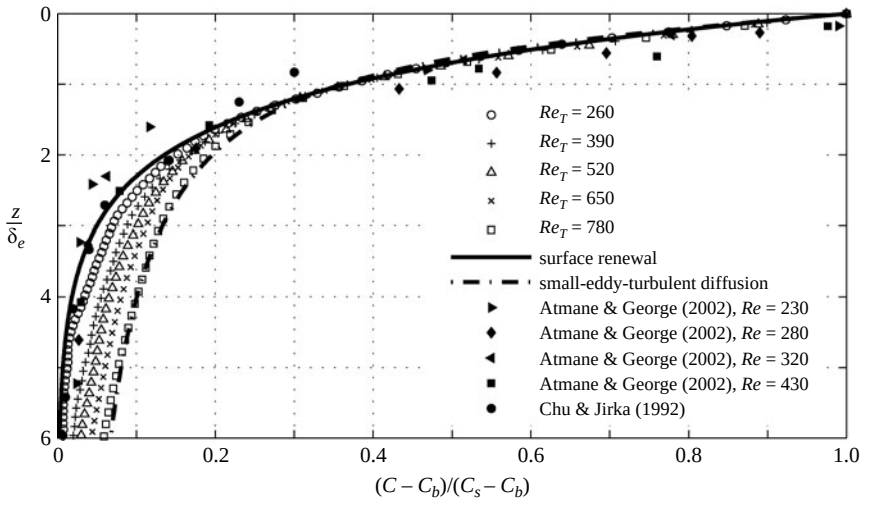


FIGURE 6. Normalized mean concentration profiles. Only every seventh data point is shown. The figure highlights the advantage of the present LIF technique over the invasive point-based measurement technique used by previous studies which was limited to near the interface.

dominant eddy sizes should be asymptotic to the Kolmogorov scales. In practice, the results can be interpreted to mean that the surface renewal model (with the eddies that are larger than the boundary layer being dominant) holds better for low $Re_T$, whereas the small-eddy-turbulent diffusion model appears preferable for high $Re_T$. This supports the idea of the two-flow regime model suggested by Theofanus (1984).

3.3.2. *Fluctuation intensity profiles*

The variation of the root-mean-squared concentration fluctuations $c'_{rms}$ with the depth is shown in figure 7. The measured values are normalized with $C_s - C_b$ and the depth with $\delta_e$. The fluctuations increase from smaller values near the interface to a maximum around the boundary-layer thickness ($z/\delta_e = 1$), with the peaks ranging between 0.15 and 0.2. Below $z/\delta_e = 1$, the fluctuations decrease. Compared with Atmane & George (2002) and Chu & Jirka (1992), we were able to elucidate in more detail the vertical r.m.s. $c'$ distribution. The scattering of the observed peaks in the previous works is most probably caused by the unpredictable bias in their $c'$. The probe from both Atmane & George (2002) and Chu & Jirka (1992) was rotated on a horizontal level to obtain the statistics of the vertical concentration distributions, which means that the data points were discrete and not simultaneous. It should also be noted that this interface region is infinitely thin. Thus, it is expected that this region behaves as a singularity, especially when using invasive measurement techniques.

The present results show that the concentration fluctuations very near the interface decrease to zero towards the interface. This behaviour was also observed by Chu & Jirka (1992) and Atmane & George (2002). In contrast, Prinos, Atmane & George (1995) found an increase towards the surface. The physical explanation for the zero and non-zero value of $c'_{rms}$ at the interface is as follows. When a surface renewal effect reaches the surface (i.e. breaking up the interface), the surface concentration may drop significantly from its saturation value. This effect causes the non-zero value of $c'_{rms}$ at the interface. On the other hand, the surface concentration remains saturated when the surface renewal effect does not reach the interface and so the $c'_{rms}$ value is zero. In the present study, the fluctuation in the vicinity of the interface shows a tendency

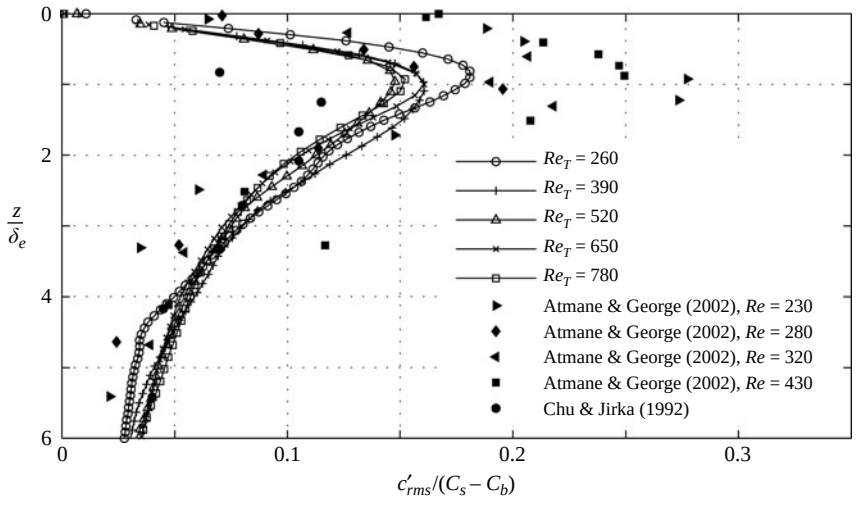


FIGURE 7. Normalized fluctuation concentration profiles. Only every seventh data point is shown. The unconnected data points are probably biased owing to the optical blurring correction procedure in the image processing. The discrepancies with previous studies might be due to their invasive measurement techniques. The interface region is infinitely thin and thus behaves as a singularity, especially when using invasive measurement techniques.

to decrease to zero towards the interfaces, as shown in figure 7. The level of certainty of the $c'_{rms}$ data extremely close to the water surface is unpredictable owing to the optical blurring correction procedure performed in the image processing (Herlina & Jirka 2004). The probably biased data points are purposely left unconnected by the solid lines in order to distinguish them from the unbiased data points. From visual observations, a distinct boundary layer could be detected in all the raw LIF images recorded in the present study. In other words, the surface renewal effect was never found penetrating up to the air–water boundary. This means that the surface concentration is expected to be always at saturation. Therefore, the tendency towards zero for the concentration fluctuations near the surface shown in figure 7 is most probably a real physical effect at least for the present range of turbulent Reynolds number ($Re_T = 260$ to 780).

### 3.4. *Velocity fluctuations near the interface*

The profiles of the root mean squared horizontal and vertical velocity fluctuations in the vicinity of the water surface are presented in a normalized form in figure 8(*a*) and 8(*b*), respectively. The measured $u'_{rms}$ and $w'_{rms}$ are scaled with their values at $z = 20$ mm, while $z$ is normalized with $z_s$. The solid lines are the fitted relations proposed by Brumley & Jirka (1987) that are based on the Hunt & Graham (1978) theoretical predictions. The profile shapes mainly conform to the Hunt & Graham theory, except for the horizontal fluctuations very near to the surface between $z/z_s =$ 0 and 2 %. Here, the measured $u'_{rms}$ constantly decrease when approaching the surface whereas the Hunt & Graham theory predicts an increase. Previous experimental data from Brumley & Jirka (1987) showed the same behaviour as our present data. The reason for the deviation from the theory is that the Hunt & Graham irrotational source theory does not take into account several second-order effects. The purely kinematic Hunt & Graham theory assumes a uniform (i.e. constant with depth) dissipation rate even in the theoretical source layer. It also assumes that the smallest

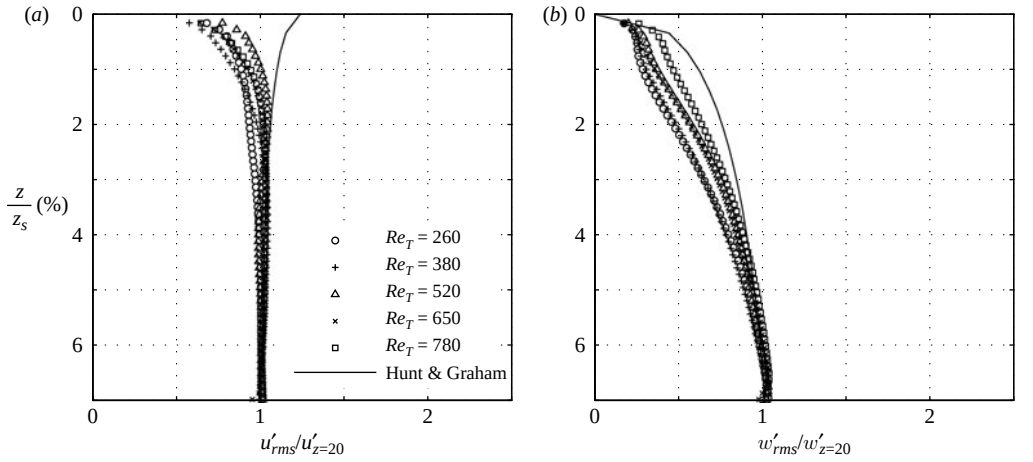


FIGURE 8. Normalized turbulence fluctuations near the interface, only every second data point is shown. The profile shapes mainly conform to the Hunt & Graham profile, except for the horizontal fluctuations extremely near the water surface. Here, the experimental data show the existence of a viscous boundary layer, which is not considered by the Hunt & Graham theory. (*a*) Horizontal fluctuation; (*b*) vertical fluctuation.

eddies near the surface are of the same size as the smallest eddies in isotropic turbulence. With their assumptions, the surface effect modifies the velocity spectra at low wavenumbers, but the inertial subrange of wavenumbers associated to length scales smaller than the depth and larger than the Kolmogorov scale is supposed to be unaffected. However, this may not be the case, as indicated by the dissipation rate profiles measured by Brumley (1984). Anisotropic straining may transfer energy from the vertical to the horizontal component even in the inertial subrange. Furthermore, the Hunt & Graham theory does not consider the existence of a viscous boundary layer, which following the estimation from Brumley & Jirka (1987), $L_\nu = L_\infty Re_T$, should range between $z/z_s = 0.4$ and 0.6 %. The low horizontal velocity fluctuations measured when approaching the interface, on the other hand, indicate the existence of a viscous boundary layer in the present experiments. At a clean interface, the viscous boundary layer mostly affects the horizontal velocity. Therefore, the Hunt & Graham theory predicts the distribution of the vertical velocity fluctuation better than the horizontal one.

### 3.5. *Oxygen transfer velocity* ($K_L$)

Before discussing the turbulent mass flux $c'w'$, independent benchmark data on the transfer velocity $K_L$, determined through long-time oxygen concentration measurements in the bulk, are presented. For these reaeration experiments, the oxygen concentration was first lowered by bubbling nitrogen and then the concentration increase was monitored for approximately 3 h using an oxygen sensor (InoLab Level 3).

The integration of the conservation of mass equation ($\mathrm{d}C_b/\mathrm{d}t = K_L/H(C_s - C_b)$) with an initial condition $(C_s - C_b)_o$ at time $t = t_o$ yields

$$\ln(C_s - C_b)_o - \ln(C_s - C_b) = \frac{K_L}{H}(t - t_o), \tag{3.2}$$

where $H$ is the water depth. When plotting the measured oxygen concentration increase against time in the form of (3.2), the gradients of the curves give the

| Experiment number | $Re_T$ | $K_2$ ($1\,s^{-1}$) ($\times 10^{-6}$) | $H$ (cm) | $K_{L,t}$ ($cm\,s^{-1}$) ($\times 10^{-4}$) | $K_{L,\delta e}$ ($cm\,s^{-1}$) ($\times 10^{-4}$) |
|---|---|---|---|---|---|
| Cb1 | 260 | 8.55 | 48.6 | 4.16 | 2.80 |
| Cb2 | 390 | 11.51 | 48.5 | 5.58 | 4.27 |
| Cb3 | 520 | 14.07 | 48.5 | 6.82 | 4.95 |
| Cb4 | 650 | 16.18 | 49.0 | 7.93 | 5.11 |
| Cb5 | 780 | 19.79 | 48.0 | 9.50 | 5.57 |

TABLE 2. $K_L$ values with varying turbulence intensities. $K_{L,t}$ is the absolute tansfer velocity coefficient determined from the bulk measurement. $K_{L,\delta e} = D/\delta_e$ is the estimated transfer velocity using the film model.

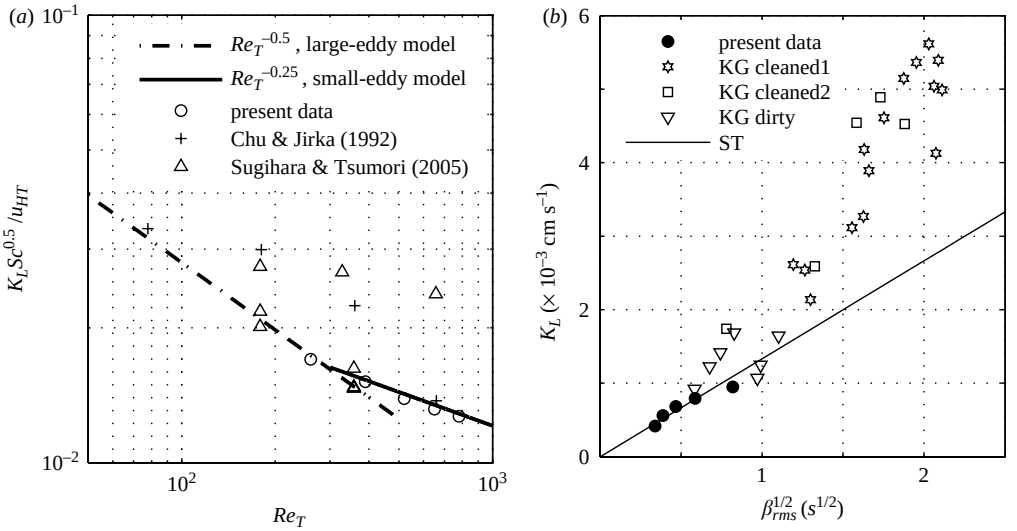


FIGURE 9. Variation of the transfer velocity $K_L$. (*a*) Variation of normalized $K_L$ with the turbulent Reynolds number $Re_T$. The data generally follow the exponent dependency of $-0.25$ (small-eddy model). (*b*) Variation of $K_L$ with a measure of surface divergence. KG and ST represents the data from McKenna & McGillis (2004*b*) and Sugihara & Tsumori (2005), respectively. The $K_L$ values from KG are normalized to $K_L$ for $Sc = 500$.

depth-averaged transfer velocities $K_L/H$. In the environmental engineering literature, $K_L/H$ is often referred to as the reaeration coefficient $K_2$. Table 2 shows the measured transfer velocities $K_{L,t}$ at a reference temperature of 20 °C. A correction factor of 1.0241 (Churchill 1961) is used for the temperature $T$ differences ($K_L(T) = K_{L,20} \times 1.0241^{(T-20)}$). For comparison, the transfer velocities estimated based on the film model $K_{L,\delta e} = D/\delta$ (Lewis & Whitman 1924) using the measured $\delta_e$ are included in table 2. The calculated $K_{L,\delta_e}$ values are underestimated compared to the measured ($K_{L,t}$) values. The presence of turbulence causes constant change of the boundary-layer thickness and may transport portions of oxygen-rich layers into the bulk. The film model oversimplifies these actual mechanisms, thus accurate prediction can not be expected.

Figure 9(*a*) shows the measured $K_L$ values in a normalized form ($K_L Sc^{0.5}/u_{HT}$) plotted against $Re_T$ on double-logarithmic axes. The present data generally follow the exponent dependency of $-0.25$ (small-eddy model). Previous data obtained by

Chu & Jirka (1992) and Sugihara & Tsumori (2005) are included in the graph. However, large scattering is observed although the turbulence generation and the definition of the turbulent Reynolds number $Re_T$ are the same. This might be the effect of surface films. One major difficulty in comparing $K_L$ values measured in different facilities is that the degrees of surface contamination are usually not reported. McKenna & McGillis (2004*b*) showed that the presence of surface films in grid-stirred tank systems reduces the transfer velocity significantly compared with cleaned surface cases. The two extreme surface conditions may be characterized by either zero velocity fluctuations (solid interface) or zero shear stress (mobile interface). The latter represents a clean interface. In our experiments, the surface was cleaned using a suction device prior to each measurement. With this procedure, we were able to maintain relatively the same surface conditions for the experiments with different $Re_T$. Despite the careful precaution taken, it was impossible to maintain a perfectly clean surface condition throughout the experiment (lasting 3 h). However, the non-zero horizontal velocity fluctuations measured at the interface (figure 8) indicate that the surface conditions were far from the extreme case of solid interface. Banerjee *et al.* 2004, McKenna & McGillis 2004*b* and Sugihara & Tsumori 2005, for example, have found that the surface divergence provides a better relationship for the gas transfer which takes into account the effect of surface conditions. In the present study, the long-time oxygen measurements were not accompanied by concurrent PIV measurements so that accurate examination of the $K_L$ dependence on the surface divergence could not be performed. However, if the surface conditions during the long-time bulk measurements and the near-surface PIV-LIF measurements are the same, the surface divergence should be more or less the same. With this assumption, the $K_L$ values are plotted against a measure of the surface divergence $\beta$ in figure 9(*b*). Here, $\beta$ is computed from the surface-normal velocity gradients measured nearest to the interface ($\beta = \partial w/\partial z$). The symbol $\beta_{rms}$ denotes the root mean squared value of the instantaneous $\beta$. The plot shows that the present data support the surface divergence model. As our study focuses on elucidating the vertical plane, we do not include further detailed discussion related to surface divergence.

### 3.6. *Turbulent mass flux*

#### 3.6.1. *Instantaneous turbulent mass flux*

We can look at the instantaneous fluctuation data in order to understand the interaction between the eddy motions and the gas transfer process. Representative time histories of the simultaneously measured concentration fluctuation and velocity fluctuation, as well as their normalized cross-product at selected points from CV1 with $Re_T = 260$, are shown in figure 10. In the graph, the measured turbulent mass fluxes are normalized by the mean flux ($\overline{j} = K_L(C_s - C_b)$) determined from the reaeration experiments (table 3). Figure 10(*a*) represents the measurement point nearest to the interface ($z = 0.074$ mm), whereas figure 10(*b*) is further away from the interface ($z = 1.094$ mm). The concentration extremely near the interface fluctuates more weakly when compared to the one measured at $z = 1.094$ mm. This is consistent with the observation of an almost undisturbed interface in the present experiments. At this level, the transfer is dominated by molecular diffusion and the turbulent transport term is almost zero in the mean ($\overline{c'w'}/\overline{j}$). Sufficiently far from the interface, the instantaneous $c'w'$ fluctuates energetically and can reach values up to two orders of magnitude larger than the absolute mean flux $\overline{j}$.

A downward flux that represents an oxygen transfer from the air into the water body occurs when both fluctuations are correlated ($w' > 0$, $c' > 0$ or $w' < 0$, $c' < 0$). As

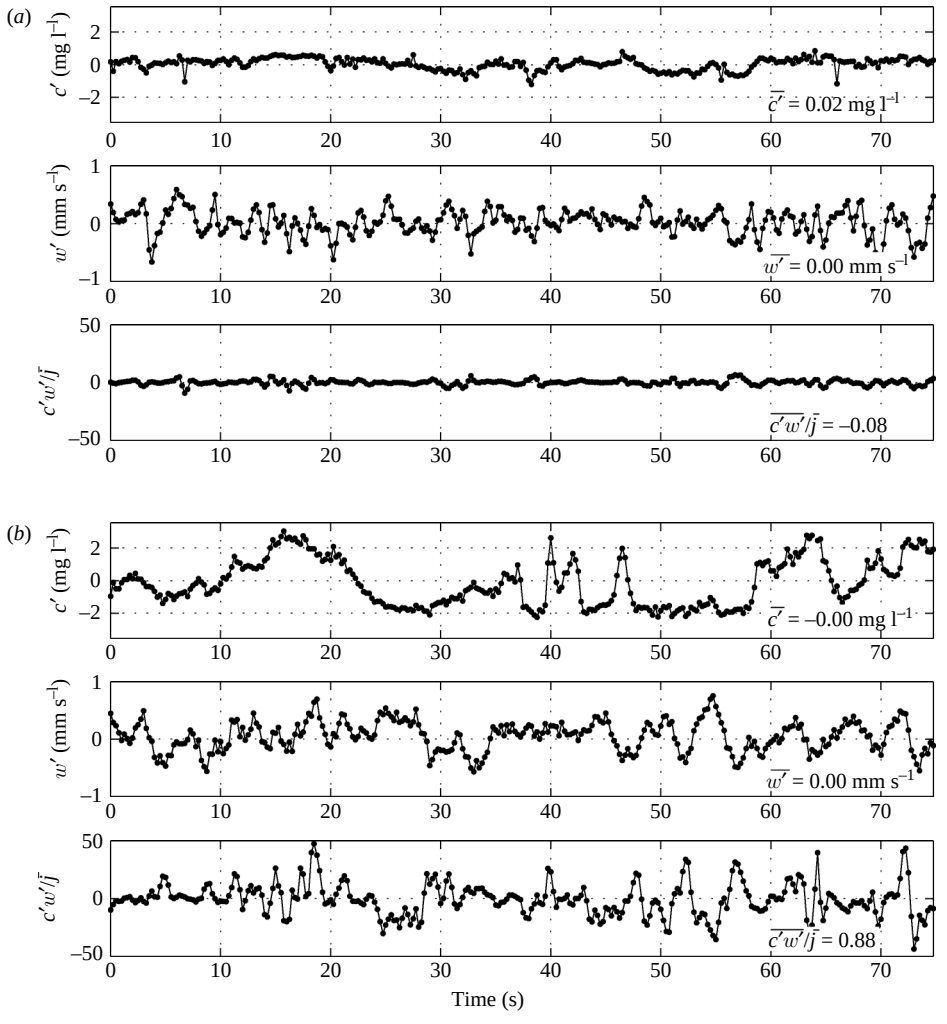


FIGURE 10. Time history of the simultaneously measured $c'$ and $w'$ and their normalized cross-correlation at selected points with $Re_T = 260$. (*a*) $x = 253.7$ mm, $z = 0.074$ mm; (*b*) $x = 253.7$ mm, $z = 1.094$ mm. The plots of $w'$ and $c'w'$ show smoothed values over five instantaneous values.

depicted in figure 10, the concentration fluctuations $c'$ are not always correlated with the vertical velocity fluctuations $w'$ ($w' > 0$, $c' < 0$ or $w' < 0$, $c' > 0$), resulting in an upward flux. In the mean and sufficiently far from the interface, a downward (positive) net flux for the mean turbulent mass flux $\overline{c'w'}$ that equals the mean flux $\bar{j}$ across the interface should be expected. A physical explanation for the positive fluxes and the negative fluxes has been discussed by Atmane & George (2002). For the present case, the positive fluxes are related to the surface renewal events where portions of fluid with lower oxygen concentration ($c' < 0$) from the bulk are being transported towards the surface by upwelling eddy motions ($w' < 0$), stay long enough to allow a diffusion process to take place, and then these portions with yet higher oxygen concentration ($c' > 0$) return to the bulk by downwelling eddy motions ($w' > 0$). When the diffusion time (at the surface or in the bulk) is too short for the fluid packages to exchange gases, the fluid packages return to their initial positions without bringing or losing a

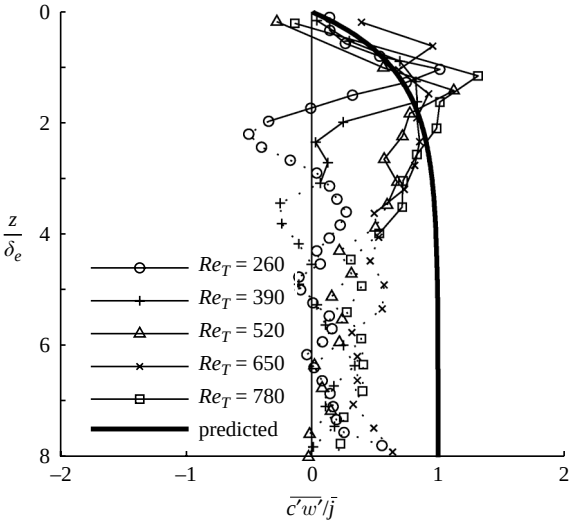


FIGURE 11. Variation of mean turbulent mass flux with depth. The mean turbulent fluxes $\overline{c'w'}$ are normalized by the total mean flux $\overline{j}$ determined from the bulk measurements. The data points in the region where the results of the eddy-correlation are biased by the poor accuracy are connected by dashed lines instead of solid lines.

| Experiment number | $Re_T$ | $T$ (°C) | $K_{L,t}$ at 20°C ($\mathrm{cm\,s^{-1}}$) ($\times 10^{-4}$) | $C_s$ ($\mathrm{mg\,l^{-1}}$) | $C_b$ ($\mathrm{mg\,l^{-1}}$) | $\overline{j}$ ($\mathrm{mg\,l^{-1}} \times \mathrm{cm\,s^{-1}}$) ($\times 10^{-4}$) |
|---|---|---|---|---|---|---|
| CV1 | 260 | 14.3 | 4.16 | 10.12 | 1.02 | 33.8 |
| CV2 | 390 | 14.4 | 5.58 | 10.10 | 0.97 | 45.9 |
| CV3 | 520 | 14.8 | 6.82 | 10.09 | 0.98 | 54.2 |
| CV4 | 650 | 15.0 | 7.93 | 9.96 | 0.77 | 64.7 |
| CV5 | 780 | 15.3 | 9.50 | 9.90 | 0.89 | 75.7 |

TABLE 3. Total mean flux values determined from the bulk measurements (reaeration experiments) $\overline{j} = K_L(C_s - C_b)$.

significant amount of oxygen and its contribution to gas exchange is negative (upward flux).

### 3.6.2. *Mean profile of turbulent mass flux*

The variation of the mean turbulent mass flux $\overline{c'w'}$ is presented in figure 11. The depth is normalized with the measured boundary-layer thickness $\delta_e$ and the mean turbulent fluxes $\overline{c'w'}$ are normalized by the total mean flux $\overline{j}$ (as given in table 3) determined from the independent bulk measurements. For all five $Re_T$, the normalized turbulent fluxes increase from around 0 at the interface to about 1 within approximately $2\delta_e$. This agrees with the fact that in the immediate vicinity of the water surface any turbulent transport should vanish and molecular diffusion is the dominant transfer mechanism. Also shown in figure 11 is the predicted turbulent flux distribution (indicated by the solid line) assuming a constant flux model in the surface region. The predicted profile is obtained by subtracting the molecular flux $-D\partial\overline{c}/\partial z$ from the total mean flux $\overline{j}$ and $\overline{c}$ is assumed to follow an exponential function. In

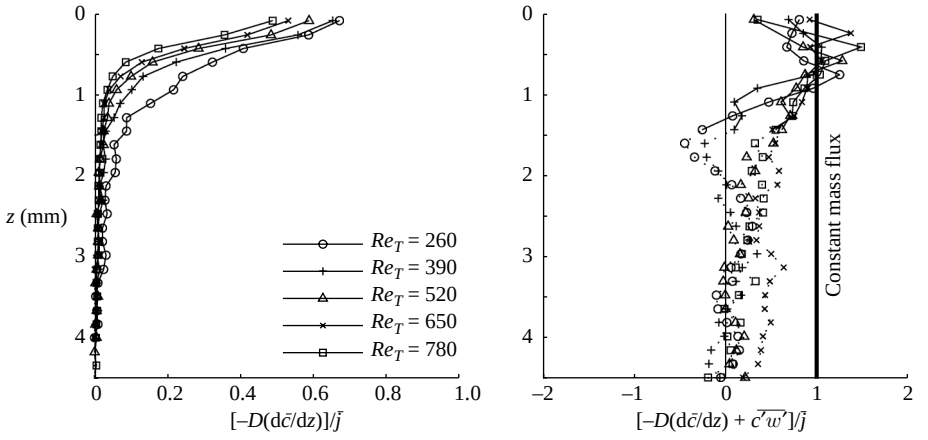


FIGURE 12. (*a*) Variation of measured molecular diffusive transport with depth calculated from the vertical concentration profiles $\bar{c}(z)$ obtained using the LIF technique and (*b*) the resulting total mass flux obtained as the sum from (*a*) and figure 11. All values are normalized with the absolute total mean flux $\bar{j}$ (table 3) determined from the bulk measurements.

the surface region down to $z/\delta_e \cong 2$, the measured turbulent fluxes agree well, both in trend and magnitude, with the predicted fluxes. For the high-Reynolds-number cases $Re_T = 520$ to 780, the agreement is good down to $z/\delta_e \cong 3$. The values of $\overline{c'w'}$ are of the same order of the total mean flux determined from the bulk measurements ($\overline{c'w'}/\bar{j} \approx 1$), which shows that the contribution of the turbulent mass flux to the total gas flux is indeed significant. Such experimental evidence within the very thin surface layer, at least down to $z/\delta_e \cong 2$, has not been reported before and should be useful in testing numerical models.

Deeper in the bulk ($z/\delta_e > 3$), the measured normalized fluxes tend to decrease to zero, which of course should not be the case. At all regions sufficiently far from the surface, pure turbulent flux should occur (i.e. $\overline{c'w'}/\bar{j} = 1$). Although the mean concentration fluctuations in the almost fully mixed bulk region tend to reach zero ($c'_{rms} \to 0$), the multiplication of the instantaneous $c'$ and $w'$, should still be something finite ($c'w' \neq 0$). The discrepancy with the theory is due to the strong attenuation of the LIF laser light as it travels through the water column. Thus, the detection of the minute $c'$ becomes more obscure with further submergence. In other words, the present LIF accuracy is insufficient in the deeper bulk region, as far as the eddy-correlation method is concerned.

### 3.7. *Total mean flux*

The total mass flux can be determined directly from the measurements by adding the molecular diffusive transport and the turbulent mass transport terms (see equation (1.1)). The first term $-D\partial\bar{c}/\partial z$, which can be quantified from the vertical concentration profiles $\bar{c}(z)$ (figure 6) is shown in figure 12(*a*). The sum of these two terms, the total mean flux, is shown in figure 12(*b*). All values are normalized by the total mean flux $\bar{j}$ determined from the independent bulk measurements (table 3). The profiles in figure 12(*a*) clearly show that molecular diffusion is the dominant transfer mechanism in the immediate vicinity of the water surface and its contribution decreases with further submergence into the bulk.

In the upper surface region, it could be shown in figure 12(*b*) that the total mass flux agrees well with the total flux $\bar{j}$ determined from the bulk measurements (i.e.

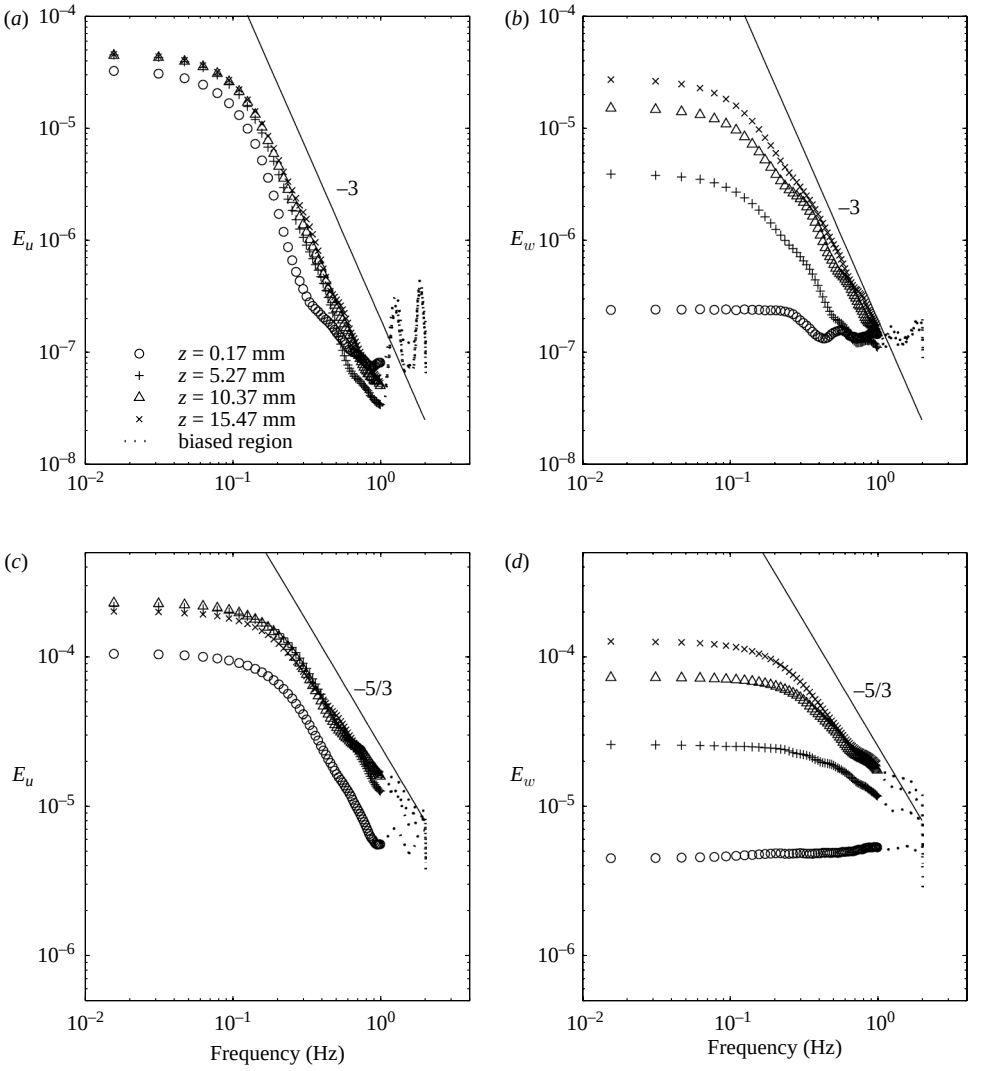


FIGURE 13. Spectra of near-surface velocity fluctuation for $Re_T = 260$ and 780. (*a*) $E_u$ for $Re_T = 260$. (*b*) $E_w$ for $Re_T = 260$. (*c*) $E_u$ for $Re_T = 780$. (*d*) $E_w$ for $Re_T = 780$.

$-D\partial\overline{c}/\partial z + \overline{c'w'} \approx \overline{j}$). The apparent success in revealing these quantities shows that the present measurement technique works successfully within the very thin surface layer. As it goes deeper into the bulk, the total flux measured using the eddy-correlation method begins to deviate from the actual constant mass flux. The discrepancy is due to the limited accuracy of the measured $\overline{c'w'}$ in the deeper bulk region, as has been discussed in § 3.6.2.

### 3.8. *Spectra*

Although the spectral analysis in this study is limited to a lower-frequency range owing to the restricted sampling frequency of 4 Hz, an attempt to interpret the spectra is given. The velocity spectra at selected submergence levels $z$ for the case with the lowest and highest $Re_T$ are shown in figure 13. The peaks at and around 1–2 Hz observed in the spectra of the velocity fluctuations are caused by the noise related to the grid

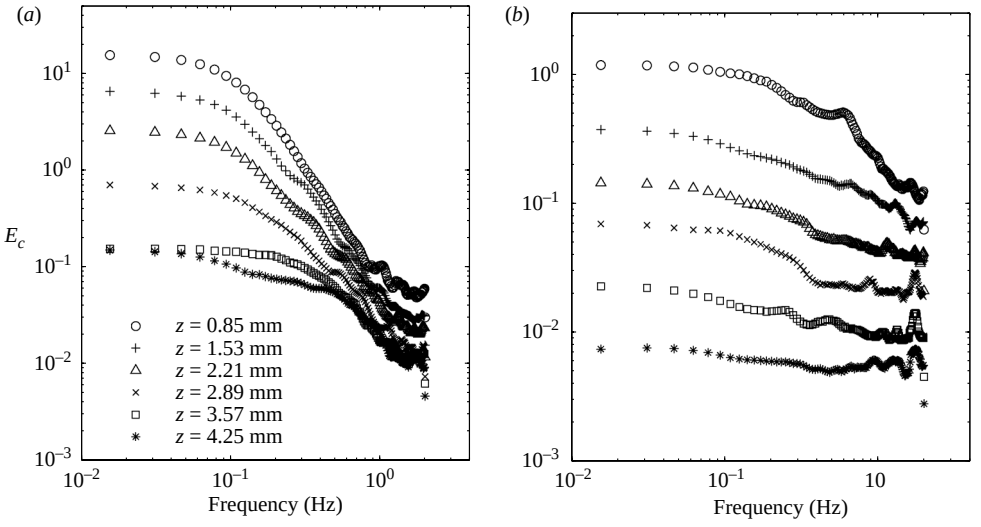


FIGURE 14. Spectra of concentration fluctuation $c'$. (*a*) $Re_T = 260$, (*b*) 780.

oscillation frequencies and not to any turbulence production. In the figures, these biased regions are indicated by the dotted lines. The velocity spectra indicate that the turbulent kinetic energy increases with increasing submergence. For the case with the lower $Re_T$, the spectra near the surface region mostly follow a slope of $-2$ or $-3$, whereas in the bulk region they follow a slope of $-5/3$ (Herlina 2005). The slope of $-5/3$ is representative of the inertial subrange in three-dimensional turbulence, which is the case in the bulk region. However, this is not the case when the near-surface region is approached. Here, the flow motion in the vertical direction is restricted and the flow becomes more two-dimensional. The inertial subrange for two-dimensional turbulence flow is characterized by a slope of $-3$ (Batchelor 1969). The $-2$ slope may be related to the stretching of the turbulent eddies from three dimensions in the bulk to two dimensions as they approach the surface. Comparing the vertical velocity spectra with the horizontal spectra, we can observe the strong damping effect of the water surface on the vertical fluctuation components. The turbulent energy of the vertical velocity fluctuations (figures 13*b* and 13*d*) decreases rapidly towards the surface; within about 15 mm from the surface, the energy decreases almost by an order of $10^2$. On the other hand, within the same submergence, the turbulent energy of the horizontal component stays at about the same order of magnitude. This shows that the vertical fluctuation components are inhibited by the surface, whereas the horizontal fluctuations may develop freely.

The concentration spectra at selected submergence obtained for the lowest and highest $Re_T$ numbers are shown in figures 14(*a*) and 14(*b*), respectively. In contrast to the velocity spectra, the concentration spectra indicate that the concentration fluctuations decrease with submergence, as expected.

The spectral density functions of the turbulent mass flux ($E_{cw}$) at selected depth for the lowest and highest $Re_T$ numbers are shown in figure 15. The spectral density illustrates how much the cross-product of $c'$ and $w'$ contributes to the gas transfer at a certain frequency. In the deeper bulk region, the measured $\overline{c'w'}$ are biased by the poor accuracy of the eddy-correlation method, as discussed in § 3.6.2. In all $Re_T$ cases, the energy spectra decreases with deeper submergence. For the lower turbulence level measured ($Re_T = 260$ and 390) depicted in figure 15(*a*) and 15(*b*), there is a decrease

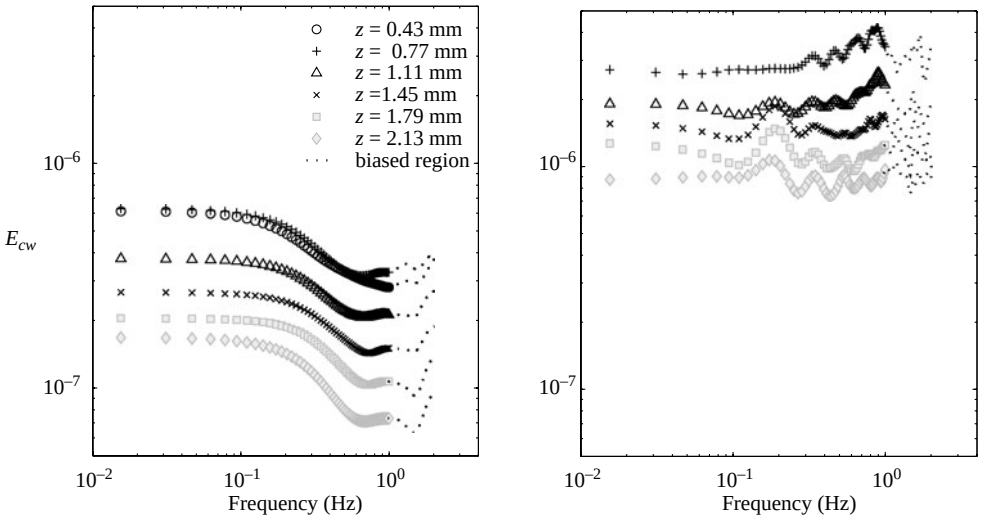


FIGURE 15. Spectra of turbulent mass flux $c'w'$. The spectra with limited accuracy (i.e. the ones in the deeper region) are shaded light grey. (*a*) $Re_T = 260$, (*b*) 780.

of energy from the lower frequencies (large eddy) to higher frequencies (small eddy). Ignoring the noise peaks at 1–2 Hz, the spectra for the lower $Re_T$ indicate that the gas flux is dominated by the large eddies. Such a clear trend could not be found in the spectra for the other cases with higher $Re_T$. For the case with the highest $Re_T = 780$, there is a tendency for the higher (small-eddy) frequencies to be more dominant (figure 15*b*).

## 4. Conclusions

The gas transfer across the air–water interface in a turbulent environment induced by an oscillating grid was investigated through detailed measurements near the interface using a combined PIV-LIF technique that enables synoptic measurements of velocity and concentration fields. From the visual observations of the instantaneous concentration maps, there is an indication that both eddy sizes play an important role in the gas transfer process. Further statistical analysis shows that the normalized mean concentration profiles for all five measured turbulent Reynolds numbers ($Re_T = 260$ to 780) fall between the two theoretical profiles based on the surface renewal model with dominant-large-scale assumption and the small-eddy turbulent diffusion model reported in Jähne & Haussecker (1998). The measured profiles clearly show the tendency that as the turbulent Reynolds number increases, the spatial drop-off of the normalized concentration profile into the bulk is slower (see figure 6). This indicates that the spectral distribution of turbulent kinetic energy between the small and large scales, as indicated by $Re_T$, plays a significant role in gas transfer. The measured transfer velocities $K_{L,t}$ values obtained from the bulk measurements generally follow the exponent dependency of $-0.25$ (small-eddy model). The spectra of the covariance term $c'w'$ indicate that the contribution of $c'w'$ is larger in the lower-frequency region for cases with small $Re_T$, whereas for the other cases with higher $Re_T$, the contribution of $c'w'$ appears to be larger in the higher-frequency region (small eddies). All these interrelated facts suggest that the gas transfer process is controlled by a spectrum of different eddy sizes and that the gas transfer at different turbulence levels can be

associated with certain eddy sizes. For very high turbulence levels, the gas transfer appears to be dominated by the small-scale eddies, whereas for very low turbulence level by the large-scale turbulent structures.

The normalized turbulent flux $\overline{c'w'}$ profiles increase from around 0 at the interface to about 1 within approximately $2\delta_e$, where $\delta_e$ is the mean boundary-layer thickness. The measured turbulent flux is of the same order of the total mean flux determined from the bulk measurements ($\overline{c'w'}/\overline{j} \approx 1$) and thus it could be shown that the contribution of the turbulent mass flux to the total flux is indeed significant.

A general quantitative model that provides a precise prediction of the transfer velocity in different environmental conditions has not yet been obtained, but an improved fundamental knowledge of the mechanisms that control the gas transfer process in a bottom-shear-induced turbulent environment was gained. Detailed information of the mean and fluctuation concentration characteristics, as well as the near-surface hydrodynamics, was obtained. These new experimental data will be an important additional base for the development and validation of highly resolving numerical modelling efforts (DNS or LES).

The authors wish to thank the German Science Foundation (Deutsche Forschungsgemeinschaft) for the financial support through Grants DFG Ji 18/7 and Ji 18/13.

## REFERENCES

Atmane, M. A. & George, J. 2002 Gas transfer across a zero-shear surface: a local approach. *Geophysical Monograph 127, Gas Transfer at Water Surfaces*, pp. 255–259.

Banerjee, S., Rhodes, E. & Scott, D. S. 1968 Mass transfer to falling wavy liquid films in turbulent flow. *Indust. Engng Chem. Fund.* **7**, 22.

Banerjee, S., Lakehal, D. & Fulgosi, M. 2004 Surface divergence model for scalar exchange between turbulent streams. *Intl J. Multiphase Flow* **30**, 963–977.

Batchelor, G. K. 1969 Computation of the energy spectrum in homogeneous two-dimensional turbulence. *Phys. Fluids* **12** (12), 233–239.

Brumley, B. 1984 Turbulence measurements near the free surface in stirred grid experiments. *Gas Transfer at Water Surfaces*, pp. 83–92.

Brumley, B. H. & Jirka, G. H. 1987 Near-surface turbulence in a grid-stirred tank. *J. Fluid Mech.* **183**, 236–263.

Brumley, B. H. & Jirka, G. H. 1988 Air–water transfer of slightly soluble gases: turbulence interfacial processes and conceptual models. *PhysicoChem. Hydrodyn.* **10**, 295–319.

Chu, C. R. & Jirka, G. H. 1992 Turbulent gas flux measurements below the air–water interface of a grid-stirred tank. *Intl J. Heat Mass Transfer* **35**, 1957–1968.

Churchill, M. A. 1961 Effect of water temperature on stream reaeration. *J. Sanitary Engng Div.* **5** (87), 59–71.

Danckwerts, P. V. 1951 Significance of liquid-film coefficients in gas absorption. *Indust. Engng Chem.* **43**, 1460–1467.

Donelan, M. A. & Wanninkhof, R. 2002 Gas transfer at water surfaces–concepts and issues. *Geophysical Monograph 127, Gas Transfer at Water Surfaces*, pp. 1–10.

Fortescue, G. E. & Pearson, J. R. 1967 On gas absorption into a turbulent liquid. *Chem. Engng Sci.* **22**, 187–216.

Gulliver, J. S. & Halverson, M. J. 1989 Air–water gas transfer in open channels. *Water Resour. Res.* **25**, 1783–1793.

Harriott, P. 1962 A random eddy modification of the penetration theory. *Chem. Engng Sci.* **17**, 149–154.

Herlina 2005 Gas transfer at the air–water interface in a turbulent flow environment. Doctoral thesis, Inst. Hydromech. University of Karlsruhe, University Press ISBN 3-937300-74-0.

Herlina & Jirka, G. H. 2004 Application of LIF to investigate gas transfer near the air–water interface in a grid-stirred tank. *Exps Fluids* **37**, 341–349.

Higbie, R. 1935 The rate of absorption of a pure gas into a still liquid during short periods of exposure. *AIChE Trans.* **31**, 365–390.

Hopfinger, E. J. & Toly, J. A. 1976 Spatially decaying turbulence and its relation to mixing across density interfaces. *J. Fluid Mech.* **78**, 155–175.

Hunt, J. C. R. & Graham, J. M. R. 1978 Free-stream turbulence near plane boundaries. *J. Fluid Mech.* **84**, 209–235.

Jähne, B. & Haussecker, H. 1998 Air–water gas exchange. *Annu. Rev. Fluid Mech.* **30**, 443–468.

Jirka, G. H. & Ho, A. H. W. 1990 Measurements of gas concentration fluctuations at water surface. *J. Hydaul. Engng ASLE* **116**, 835–847.

Kunugi, T. & Satake, S.-I. 2002 Direct numerical simulation of turbulent free surface flow with carbon dioxide gas absorption. *Geophysical Monograph 127, Gas Transfer at Water Surfaces*, pp. 77–82.

Lakehal, D., Fulgosi, M. & Yadigaroglu, G. 2003 Direct numerical simulation of turbulent heat transfer across a mobile, sheared gas–liquid interface. *Trans. ASME*: *J. Heat Transfer* **125**, 1129–1139.

Lamont, J. C. & Scott, D. S. 1970 An eddy cell model of mass transfer into the surface of a turbulent liquid. *AIChE J.* **16**, 513–519.

Lewis, W. K. & Whitman, W. G. 1924 Principles of gas absorption. *Indust. Engng Chem.* **16**.

McCready, M. J., Vassiliadou, E. & Hanratty, T. J. 1986 Computer-simulation of turbulent mass-transfer at a mobile interface. *AIChE J. Chem. Engng Res. Dev.* **32**, 1108–1115.

McKenna, S. P. & McGillis, W. R. 2002 Surface divergence and air–water gas transfer. *Geophysical Monograph 127, Gas Transfer at Water Surfaces*, pp. 129–134.

McKenna, S. P. & McGillis, W. R. 2004*a* Observations of flow repeatability and secondary circulation in oscillating grid-stirred tank. *Phys. Fluids* **16** (9), 3499–3502.

McKenna, S. P. & McGillis, W. R. 2004*b* The role of free-surface turbulence and surfactants in air–water gas transfer. *Intl J. Heat Mass Transfer* **47**, 539–553.

Magnaudet, J. & Calmet, I. 2006 Turbulent mass transfer through a flat shear-free surface. *J. Fluid Mech.* **553**, 155–185.

Matsunaga, N., Sugihara, Y., Komatsu, T. & Masuda, A. 1999 Quantitative properties of oscillating-grid turbulence in a homogeneous fluid. *J. Fluid Dyn. Res.* **25**, 147–165.

Moog, D. B. & Jirka, G. H. 2002 Air–water gas transfer in uniform flows with large gravel-bed roughness. *Geophysical Monograph 127, Gas Transfer at Water Surfaces*, pp. 371–376.

Münsterer, T., Mayer, H. J. & Jähne, B. 1995 Dual-tracer measurements of concentration profiles in the aqueous mass boundary layer. *Air–Water Gas Transfer : 3rd Intl Symp. on Air–Water Gas Transfer*, pp. 637–648.

O'Connor, D. J. & Dobbins, W. E. 1956 The mechanism of reaeration in natural streams. *J. Sanitary Engng* **82** (SA6), 1115–1140.

Pan, Y. & Banerjee, S. 1995 A numerical study of free surface turbulence in channel flow. *Phys. Fluids* **7**, 16491664.

Plate, E. J. & Friedrich, R. 1984 Reaeration of open channel flow. *Gas Transfer at Air–Water Interfaces*, pp. 333–346.

Prinos, P., Atmane, M. & George, J. 1995 Gas flux measurements and modelling below an air–water interface. *Proc. 3rd Intl Symp. Air–Water Gas Transfer*, pp. 49–57.

Roy, A. G., Buffin-Bélanger, T., Lamarre, H. & Kirkbride, A. D. 2004 Size, shape and dynamics of large-scale turbulent flow structures in a gravel-bed river. *J. Fluid Mech.* **500**, 1–27.

Sugihara, Y. & Tsumori, H. 2005 Surface-renewal eddies at the air–water interface in oscillating-grid turbulence. In *Enviromental Hydraulics and Sustainable Water Management* (ed. J. H. W. Lee & K. M. Lam), pp. 199–205.

Tamburrino, A. & Gulliver, J. S. 2002 Free-surface turbulence and mass transfer in a channel flow. *AIChE J.* **48**, 2732–2743.

Thackston, E. L. & Krenkel, P. A. 1969 Reaeration prediction in natural streams. *J. Sanitary Engng Div. Proc. ASCE* **95**(SA1), 65–93.

Theofanus, T. G. 1984 Conceptual models of gas exchange. *Gas Transfer at Air–Water Surfaces*, pp. 271–281. Reidel.

Theofanus, T. G., Houze, R. N. & Brumfield, L. K. 1976 Turbulent mass transfer at free, gas liquid interfaces with applications to open channel, bubble and jet flows. *Intl J. Heat Mass Transfer* **19**.

Thompson, S. M. & Turner, J. S. 1975 Mixing across an interface due to turbulence generated by an oscillating grid. *J. Fluid Mech.* **67**, 349–368.

Turney, D. E., Smith, W. C. & Banerjee, S. 2005 A measure of near-surface fluid motions that predicts air–water gas transfer in a wide range of conditions. *Geophys. Res. Lett*. **32** (4).

Vaughan, W. M. & Weber, G. 1970 Oxygen quenching of pyrenebutyric acid fluorescence in water, a dynamic probe of the microenvironment. *Biochemistry* **9**, 464–473.

Wolff, L. M. & Hanratty, T. J. 1994 Instantaneous concentration profiles of oxygen accompanying absorption in a stratified flow. *Exps Fluids* **16**, 385–392.

Woodrow, P. T. & Duke, S. R. 2002 LIF measurements of oxygen concentration gradients along flat and wavy air–water interfaces. *Geophysical Monograph 127, Gas Transfer at Water Surfaces*, pp. 83–88.